Gravity currents flowing upslope: laboratory experiments and shallow-water simulations

V. Lombardi[1], C. Adduce[1a)], G. Sciortino[1] and M. La Rocca[1]

[1]*Department of Engineering, University Roma Tre, Rome, 00146, Italy*

This paper investigates the dynamics of lock-release gravity currents propagating upslope by laboratory experiments and shallow-water simulations. Both the interface between the dense and the ambient fluid and the instantaneous velocity field were measured by image analysis. Different runs were carried out by varying the initial density of the lock fluid and the bed upslope. As a gravity current moves upslope, the dense layer becomes thinner, and an accumulation region of dense fluid in the initial part of the tank occurs. The current speed decreases as the bed upslope increases and for the highest up sloping angles the gravity current stops before reaching the end of the tank. A new two-layer shallow-water model is developed and benchmarked against laboratory experiments. The present model accounts for the mixing between the two layers, the free surface and the space-time variations of the density. The effect of the horizontal density gradient in the simulation of gravity currents is investigated by comparing the numerical results of both the present model and the model proposed by Adduce *et al.* [J. Hydraulic Eng., 138, 111-121 (2012)] with laboratory measurements. The comparison shows that the present model reproduces both the current shape and the front position better than the Adduce *et al.* model, in particular for gravity currents flowing up a slope. For these currents the presence of a backflow near the lock is shown by the analysis of the streamwise depth-averaged velocity predicted by the present model and the velocity measured by particle image velocimetry (PIV) as well.

I. INTRODUCTION

A gravity current is a flow driven by the density gradient between two fluids, i.e. the ambient fluid and the current itself. In its typical configuration the heavier fluid with density ρ_1 propagates into a lighter ambient fluid with density ρ_2 ($\rho_2<\rho_1$). Gravity currents occur widely in both natural and industrial flows. The density difference can be due to a dissolved solute or to a difference in temperature between the two fluids (i.e. compositional gravity currents), or to the presence of suspended sediments (i.e. particle-driven gravity currents). Examples of compositional gravity currents are sea breeze winds in the atmosphere and ocean density currents as the Mediterranean overflow, driven by the temperature and salinity gradient, respectively. Particle-driven gravity currents often occur in nature as sandstorms, avalanches, pyroclastic flows and turbidity currents (Ref. 1).

[a)] Author to whom correspondence should be addressed. Electronic mail: claudia.adduce@uniroma3.it.

Since gravity currents play an important role in many natural and artificial applications, a large amount of scientific works has been focused on this subject for decades. In particular, several authors reproduced gravity currents in the laboratory by an instantaneous release of a dense fluid, i.e. the lock-release experiment, (Ref. 2, Ref. 3, Ref. 4, Ref. 5, Ref. 6, Ref. 7, Ref. 8) or by a continuous buoyancy source (Ref. 9, Ref. 10, Ref. 11). In the lock-release configuration a tank is divided in two portions separated by a vertical sliding gate, one part is filled with lighter fluid and the other part is filled with the heavier one. The experiment begins when the gate is suddenly removed, the heavier fluid flows under the lighter one, producing the gravity current.

As well as experimental analysis, many studies employing numerical models can be found in literature. Several investigators studied gravity currents motion using high resolution Navier-Stokes numerical models as LES (Ref. 12, Ref. 13, Ref. 14), DNS (Ref. 15, Ref. 16, Ref. 17, Ref. 18) or RANS (Ref. 19). High resolution models provide a very detailed description of the gravity current dynamics, producing reliable results. However these models are very complex and require high computational resources. A recent and innovative numerical approach to investigate gravity currents is given by the application of the Lattice Boltzmann Method as in Ref. 20, Ref. 21 and Ref. 22.

Another approach commonly used to model the behavior of a gravity current is the shallow-water theory, based on the hypothesis that the vertical length scale of the flow is small with respect to the horizontal one. Usually the horizontal length scale of a typical gravity current is significantly longer than its vertical length scale, then the aspect ratio between the current depth and the whole current body is small enough to allow the application of the shallow-water theory to model the current dynamics (Ref. 23, Ref. 24, Ref. 25, Ref. 8, Ref. 26, Ref. 5). Ref. 24 proposed a shallow-water model considering the current as a two-dimensional, two-layer flow bounded at the top and at the bottom by horizontal planes and at one end by a vertical wall. They considered the partial-depth configuration, involving two inviscid, incompressible fluids with slightly different densities, and negligible mixing was assumed. Ref.

23 investigated the properties of steady gravity currents, developing an energy-conserving theory for an empty cavity advancing along the upper boundary of a liquid. Ref. 25 developed an hydraulic model for unsteady and irrotational flow. The fluid was assumed to be inviscid and immiscible, and the pressure distribution was assumed to be hydrostatic. Ref. 25 found that, for an energy-conserving current produced by a partial-depth release, the height is half of the initial height of the lock, as for the case of full-depth release proposed by Ref. 23.

The paper of Ref. 8 was focused on the effect of the bottom roughness on the dynamics of 3D gravity currents performed by laboratory experiments and numerical simulations. A 2D shallow-water model with the single layer approximation was developed and tested. A good agreement between measurements and numerical predictions of gravity current velocity and front position was observed. In Ref. 26 the authors removed the hypothesis of single layer and the prediction of the upper layer field variables was allowed. An agreement between numerical simulations and laboratory measurements was found.

Ref. 5 performed experiments with 2D lock-release gravity currents on a flat smooth bed and developed a 1D two-layer shallow-water model. Unlike previous shallow-water models, Ref. 5 removed the rigid lid approximation, considering the free surface and took into account the entrainment between the dense and the ambient fluid, by a modified Ref. 9's formula. A comparison between measurements and simulations with and without entrainment was performed and a better agreement was found when mixing was accounted for.

Regarding the geometric configuration, in addition to previous studies focused on gravity currents flowing along horizontal boundaries (Ref. 5, Ref. 7, Ref. 8), several investigations on gravity currents moving down a slope can be found in literature (Ref. 27, Ref. 28, Ref. 11, Ref. 29, Ref. 30, Ref. 31, Ref. 32, Ref. 33, Ref. 34). Comparatively, there is a small number of studies dealing with gravity currents propagating up a slope, such as Ref. 35, Ref. 36, Ref. 37 and Ref. 38. Gravity currents often occur as flows moving downslope, as avalanches, turbidity currents, pyroclastic flows. However, the dynamics of both oceanic and atmospheric gravity currents is strongly affected by the surrounding topography and a gravity current can encounter an upslope along its path. An example of a gravity current moving upslope is the estuarine salt wedge which can occur at the mouth of rivers: the sea dense water moves upstream along the river bed, while the fresh water flows seaward above the dense layer.

The present work is therefore focused on the investigation of the dynamics of gravity currents flowing upslope by laboratory experiments and shallow-water numerical simulations. The shallow-water model proposed in this paper is, on the authors' best knowledge, a novel contribution to the research on buoyancy driven flows. Indeed, starting from the model developed in Ref. 5, the following enhancements have been introduced: (i) an improved velocity scale was used to define the entrainment coefficient; (ii) the hypothesis of fluid homogeneity (i.e., the density of the gravity current can change in time but not in space) is removed leading to a further and more physically sounded equation in the governing equations. The choice of a shallow-water model has the advantage of requiring only limited computational resources. In particular, although the present model is complex enough to necessitate some numerical methods in deriving the solutions, the computational support needed is less demanding than that necessary for solving the Navier-Stokes equations using LES or DNS.

This paper is organized as follows: the experimental set-up is illustrated in section 2, results from laboratory experiments are shown in section 3, mathematical model's details are given in section 4, the comparison between experimental measurements and numerical simulations are discussed in section 5, while section 6 is devoted to the conclusions.

II. EXPERIMENTAL APPARATUS

Experiments simulating gravity currents were performed at the Hydraulics Laboratory of the University of Rome "Roma Tre", using the lock-release technique in a similar apparatus as in Ref. 39 and Ref. 6. A Perspex tank of rectangular cross-section, of depth d=0.3 m, length L=3.00 m and width

b=0.20 m was divided into two reservoirs by a vertical sliding gate, placed at a distance x_0 from the left end wall of the tank, as shown in the sketch of the experimental apparatus (Figure 1a). The left volume of the tank was filled with salty water with initial density ρ_{01} while the rest of the tank was filled with an ambient fluid of density $\rho_2 < \rho_{01}$. As full-depth, lock-release experiments were performed, both in the right and in the left part of the tank the depth of the fluid was h_0, which was measured at the gate position x_0. The tank was placed on a tilting structure in order to obtain the desired sloping angle θ.

A pycnometer was used to perform initial density measurements. The uncertainty in the density measurements was estimated as 0.2 %. The experiment started when the sliding gate was suddenly removed and the heavier fluid moved from the left part of the tank to the right part forming a gravity current. The experiment ended when the gravity current stopped propagating toward the right part of the tank.

During the experiment some dye was added to the lock fluid in order to provide the visualization of the gravity current flow as in Ref. 5 and Ref. 7. The movie of each experiment was acquired using a CCD (Charged Coupled Device) camera, with a frequency of 25 Hz and a spatial resolution of 576 × 768 pixels. An image analysis technique based on the threshold method was applied to measure the space-time evolution of the interface between the dense and the light fluid. Each frame of the movie acquired by the camera is a rectangular matrix of integers representing the grey level of the corresponding pixel, which ranges from 0 (black) to 255 (white). The grey level of the interface between the two fluids was chosen as the threshold value. Therefore the threshold value is a calibration parameter of the code, which has to be chosen in order to obtain for each experiment as output an interface between the dense and the light fluid in agreement with the acquired images. The image analysis was applied in the region of interest (725 × 50 pixels), delimited by the gate position on the left and by the end wall of the tank on the right. A ruler was positioned along both horizontal and vertical walls of the tank in order to obtain the conversion factor pixel/cm, whose value was 0.4 cm/pixel. The front position

x_f was determined from image analysis with an error of ± 0.002 m. The parameters used for the experiments are shown in Table I.

TABLE I. Experimental parameters.

Run	x_0 (m)	h_0 (m)	ρ_{01} (kg m^{-3})	ρ_2 (kg m^{-3})	r (-)	θ (°)
1	0.10	0.15	1060	1000	0.94	0.00
2	0.10	0.15	1060	1000	0.94	1.14
3	0.10	0.15	1060	1000	0.94	1.39
4	0.10	0.15	1060	1000	0.94	1.52
5	0.10	0.15	1090	1000	0.92	0.00
6	0.10	0.15	1090	1000	0.92	1.39
7	0.10	0.15	1090	1000	0.92	1.45
8	0.10	0.15	1090	1000	0.92	1.80
9[a]	0.10	0.25	1039	1011	0.97	1.36

[a]Run for which PIV measurements were performed.

Following the procedure described above, eight lock-release experiments (i.e. Run 1-Run 8) simulating gravity currents were carried out. A dyed aqueous solution of sodium chloride (NaCl) as dense fluid and fresh water as ambient fluid were used. ρ_2=1000 kg/m^3, h_0=0.15 m, x_0=0.10 m were kept constant, while two different values of density ρ_{01}=1060 Kg/m^3 and 1090 Kg/m^3, respectively, corresponding to different values of the dimensionless ratio r=ρ_2/ρ_{01}, were tested. For each density value an experiment on a flat bed and three experiments with different upslopes were carried out. In particular the gravity currents realized with the highest values of the up sloping angles (i.e. Run 4 and Run 8) stopped before reaching the right end wall of the tank.

Since shallow water numerical simulations predicted the presence of a backflow (i.e. negative values of V_1) near the lock of the tank for gravity currents flowing up a slope, PIV technique, with the RIM (Refractive Index Matching) method, was applied in order to confirm the numerical results on a physical model. As the interface between the dense and the ambient fluid is not detectable by PIV measurements, one further experiment (i.e. Run 9) was realized with the same experimental parameters and the same fluid types used for PIV measurements. This experiment was analyzed using the threshold method in order to obtain the current profile. Run 9 was performed with the following experimental parameters:

ρ_2=1011 kg/m^3, ρ_{01}=1039 kg/m^3, h_0=0.25 m, x_0=0.10 m, θ=1.36°, using an aqueous solution of glycerol as the less dense fluid and an aqueous solution of potassium dihydrogen phosphate (KH_2PO_4) as the heavier one. The choice of such fluid types is imposed by the RIM method (Ref. 40) and it will be fully explained in the following subsection A.

A. PIV experiments

The particle image velocimetry (PIV) technique was applied to perform velocity measurements for a gravity current realized by the lock-release technique with the experimental parameters corresponding to Run 9. A PIV system (Intelligent Laser Applications) with a double pulsed Nd:YAG Laser was used. The frequency between the couples of images was 3 Hz and the time between pulses was 30 ms. Both dense and ambient fluid were seeded with polyamide particles with a mean diameter of 100 μm and a density of 1016 Kg/m^3. The seeding particles were chosen in order to have an intermediate density between ρ_{01} and ρ_2. The laser sheet was positioned along the tank's centerline and a CCD camera, located normal to the laser sheet, was used to acquire couples of images in the region of interest. The PIV system is equipped with a software, based on a cross-correlation technique, which is used to obtain the velocity field.

PIV measurements were used to verify the reliability of a back flow, as it will be discussed in the following sections, predicted by the shallow-water model for all the simulated gravity currents moving up a slope. According to numerical predictions such a backflow was supposed to occur in an area near the position of the lock. Due to length's limitations in the domain acquired by the CCD camera, two PIV experiments (Run PIV1 and Run PIV2) were performed, with adjacent domains, in order to merge them in a longer domain (envelope of the domains of Run PIV1 and Run PIV2), close to the position of the lock. As shown in Figure 1b, the first field of view (i.e. Run PIV1) was 0.32 m long and started at x=0.81 m, while the second domain (i.e. Run PIV2) was 0.35 m long and started at x=1.07 m. Run PIV1 and Run PIV2 were carried out with h_0=0.25 m, which is higher than h_0=0.10 m used for Run 1-Run 8, in order to generate a thicker gravity current. This choice is ascribed to the necessity of obtaining as many as possible velocity vectors in the tail region of the gravity current, to allow a detailed observation of the area where the backflow occurred.

During the first stage of development of the gravity currents near the lock of the tank, where the investigated domains are located, there is a high density gradient between the dense fluid and the lighter one. As the index of refraction changes with the local value of the density, a high density gradient can cause a blurred image in which individual particles cannot be distinguished (Ref. 40). In order to avoid this problem the RIM method was applied. This method consists in choosing those concentrations of particular solutions which ensure a uniform refractive index throughout the flow. Following Ref. 40, a 6% aqueous solution of glycerol as the less dense fluid and a 6% aqueous solution of potassium dihydrogen phosphate (KH_2PO_4) as the heavier one were used. Such concentrations of these fluids provide about 3% of density difference and a uniform refractive index within the fluids. Therefore the values of ρ_{01}=1039 Kg/m^3 and ρ_2=1011 Kg/m^3 were imposed by the applied RIM method.

As previously pointed out, in order to identify the thickness of the gravity current for each position on the *x*-axis, an experiment (i.e. Run 9), with the same solutions and experimental parameters of Run PIV1 and Run PIV2, was performed by adding some dye to the salty water. The threshold method was applied in order to detect the interface between the two layers.

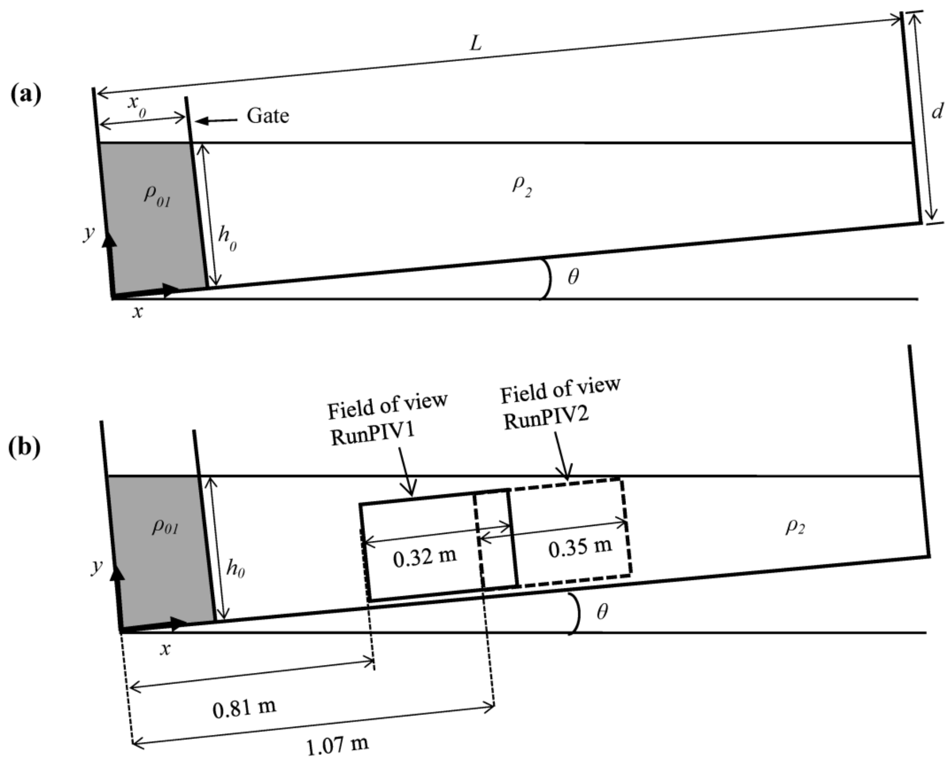

FIG. 1. Sketch of the tank used to perform laboratory experiments (a) and detailed sketch of the field of view for Run PIV1 and Run PIV2 (b).

III. EXPERIMENTAL RESULTS

In Table II values of the bulk velocity of the current front U_{fm}, the mean Reynolds number Re_m and the total depth densimetric Froude number Fr_H are shown for each released gravity current. The bulk velocity U_{fm} is obtained as the ratio between the path travelled by the current and the whole duration of the experiment and the dimensionless numbers Re_m and Fr_H were computed following Ref. 5, as:

$$\mathrm{Re}_\mathrm{m} = \frac{1}{2}\frac{U_{fm} h_0}{\nu} \tag{1}$$

$$\mathrm{Fr}_\mathrm{H} = \frac{U_{fm}}{\sqrt{h_0 g_0'}} \tag{2}$$

where ν is the kinematic viscosity of the dense fluid and $g_0{}'$ is the initial reduced gravity defined by:

$$g_0' = g\,\frac{\rho_{01} - \rho_2}{\rho_2} \tag{3}$$

in which g is the gravity acceleration.

The ranges of Re_m and Fr_H computed for all the runs ensure that in this study only turbulent and subcritical gravity currents are generated (see Table II).

Figure 2 shows the behavior of a gravity current propagating on a flat bed (i.e. Run 5) at four different times. After the gate removal the dense fluid collapses and moves to the right part of the tank along the bottom boundary, while a buoyant current (i.e. the ambient fluid) flows to the left along the upper boundary. In Figure 2 the typical features of a gravity current moving along a horizontal bed can be recognized: a head followed by a tail can be distinguished; at the interface between the two layers interfacial instabilities take place, as shown by the billows formed at the rear of the current head.

In Figure 3, the development of a gravity current moving up a slope (i.e. Run 8) is shown. The up sloping angle is large enough to make the current stop before reaching the end of the tank. As the gravity current is flowing upslope toward the right part of the tank, the dense layer becomes thinner, and an accumulation of dense fluid in the left part of the tank occurs. The head region is thin compared to the head of a gravity current flowing along a horizontal boundary. Such a behavior was observed in all the runs performed up a slope.

TABLE II. Reduced gravity, bulk velocity and dimensionless numbers

Run	g_0' ($m\ s^{-2}$)	U_{fm} ($m\ s^{-1}$)	Re_m (-)	Fr_H (-)
1	0.59	0.092	6892	0.31
2	0.59	0.063	4775	0.21
3	0.59	0.051	3810	0.17
4	0.59	0.049	3690	0.17
5	0.88	0.112	8362	0.31
6	0.88	0.079	5927	0.22
7	0.88	0.066	4942	0.18
8	0.88	0.061	4590	0.17
9[a]	0.27	0.064	7950	0.24

[a]Run for which PIV measurements were performed.

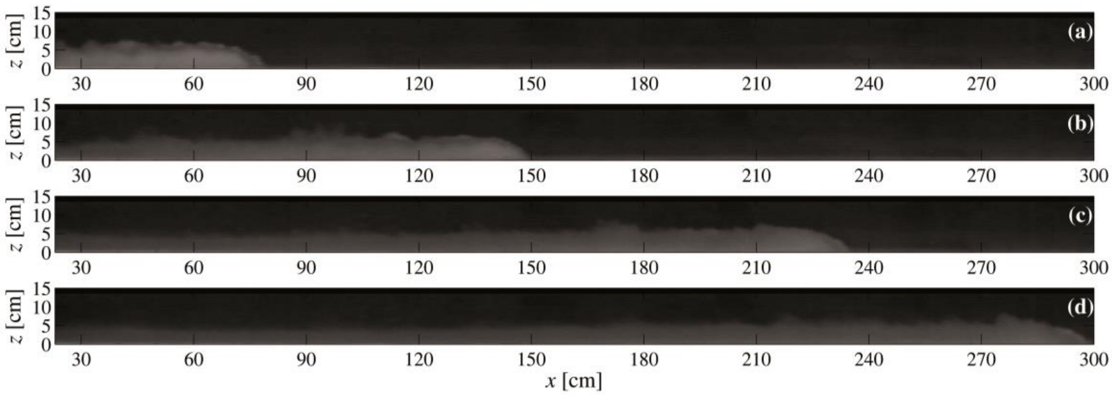

FIG. 2. Images acquired by the camera at four different times for Run 5 (flat bed): 4 s (a), 9 s (b), 17 s (c), 25 s (d).

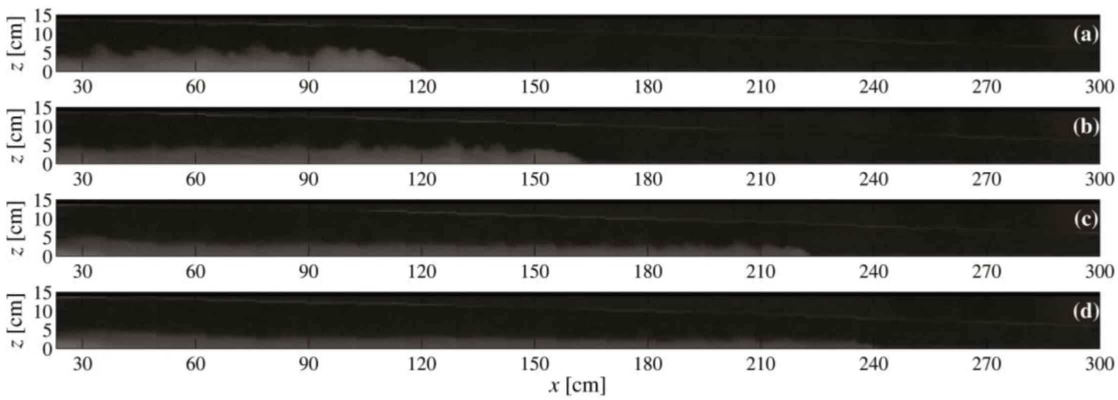

FIG. 3. Images acquired by the camera at four different times for Run 8 (θ=1.8°): 7 s (a), 11 s (b), 20 s (c), 24 s (d).

In Figure 4 and Figure 5 plots of dimensionless experimental front positions versus dimensionless time are shown for the runs characterized by ρ_{01}=1060 and 1090 Kg/m^3, respectively. Each plot shows a comparison between the runs performed with the same value of initial density of the released current and different values of the up sloping angle θ, including the run realized on a flat bed. The laboratory measurements start about 0.5 s after the gate removal. The dimensionless front position x_f^* is defined as:

$$x_f^* = \frac{x_f - x_0}{x_0} \tag{4}$$

where x_f is the instantaneous front position. Dimensionless time $T^*=t/t_0$ is defined on the basis of the time scale t_0 as:

$$t_0 = \frac{x_0}{\sqrt{g_0' h_0}} \quad (5)$$

Figures 4 and Figure 5 show, as expected, that the current speed decreases as the angle θ increases. In particular, the runs performed with the highest up sloping angles (i.e. Run 4 and Run 8) stopped before the end of the tank.

Ref. 2 and Ref. 24 investigated gravity currents generated by lock-exchange experiments in a channel of rectangular cross-section. They showed that in the dynamics of a gravity current produced by an instantaneous release of dense fluid on a horizontal bed three phases can be distinguished. The first phase, called slumping phase, is characterized by a constant speed and a linear variation of the front position with time. During the second phase, called self-similar phase, the front speed depends on time following a power law like $t^{-1/3}$ and the front position varies as $t^{2/3}$ (Ref. 24). The transition between the first and the second phase occurs when a bore, caused by the reflection of the lighter fluid on the left wall of the tank, reaches the current front, which is slower than the bore. Ref. 24 found that the transition from the first phase to the second one occurs at $x_f \cong 10 \cdot x_0$. If viscous forces are not negligible, a third self-similar phase, called viscous phase, can occur and the current speed decreases with a power law like $t^{-4/5}$, while the front position increases with $t^{1/5}$ (Ref. 41).

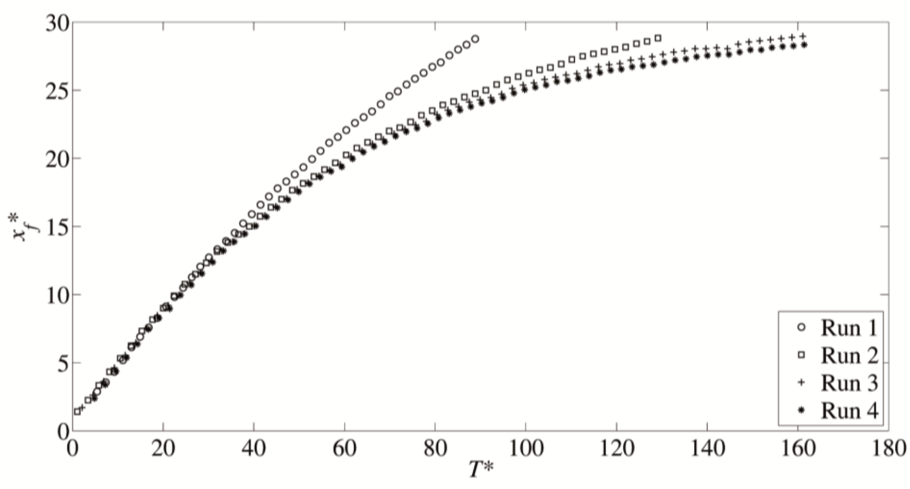

FIG. 4. Dimensionless plot of the experimental front position versus time for Runs 1-4, performed with ρ_{01}=1060 Kg/m^3 and different values of θ: 0.0° (Run 1), 0.14° (Run 2), 1.39° (Run 3) and 1.52° (Run 4), respectively.

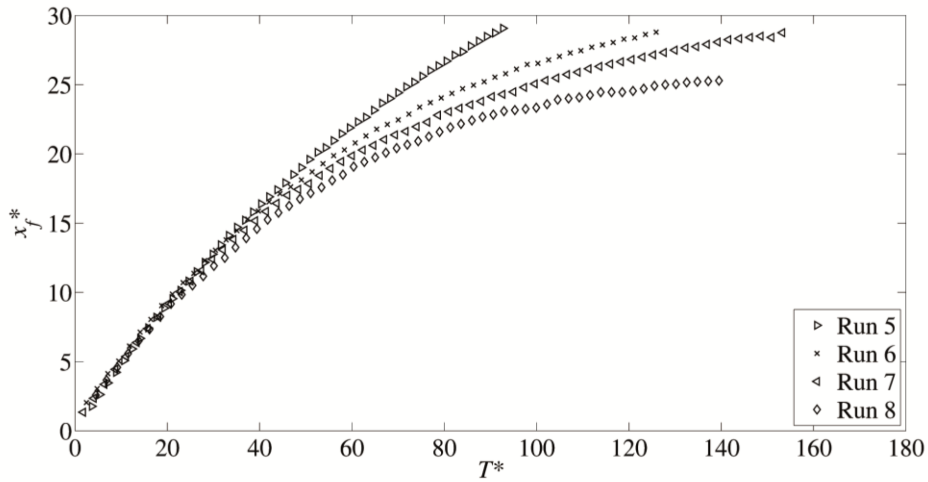

FIG. 5. Dimensionless plot of the experimental front position versus time for Runs 5-8, performed with ρ_{01}=1090 Kg/m^3 and different values of θ: 0.0° (Run 5), 1.39° (Run 6), 1.45° (Run 7) and 1.80° (Run 8), respectively.

Figure 6a shows a log-log plot of the dimensionless front positions versus dimensionless time for all the runs, together with the theoretical curves of front position given by previous studies for gravity currents propagating on a horizontal bed. Up to $x_f^* \cong 9$, i.e. when the slumping phase occurs for a gravity current realized on a flat bed, the experimental points of all the runs performed on both flat and up sloping beds collapse on the line with a slope equal to one (dashed line), showing that the first constant-speed phase is not affected by the bed upslope. However, it must be taken into account that the values of θ considered in this study are relatively small and maybe they are not high enough to influence the behavior of the current during the first phase. Beyond $x_f^* \cong 9$, i.e. when the self-similar phase occurs for a gravity current on a flat bed, the experimental points of Run 1 and Run 5 (i.e. gravity currents on a flat bed) collapse on the line with a slope of 2/3 (solid line), while the experimental points of Run 2, Run 3, Run 4, Run 6, Run 7, Run 8, i.e. gravity currents travelling upslope, first collapse towards the line with a slope 2/3, then deviate from the line of the self-similar phase tending faster to the viscous phase. The higher is the bed upslope, the lower is the slope of the tangent to the curve obtained at the end of the run.

The evolution of the experiments during the second and the third phase is shown with more detail in the close-up given in Figure 6b, where the third viscous phase seems to be reached by the currents moving up a slope. In particular Run 4 and Run 8, which were performed with the highest values of bed upslope seem to develop a viscous phase, with a slope almost equal to 1/5 (dotted line) at the end of the run.

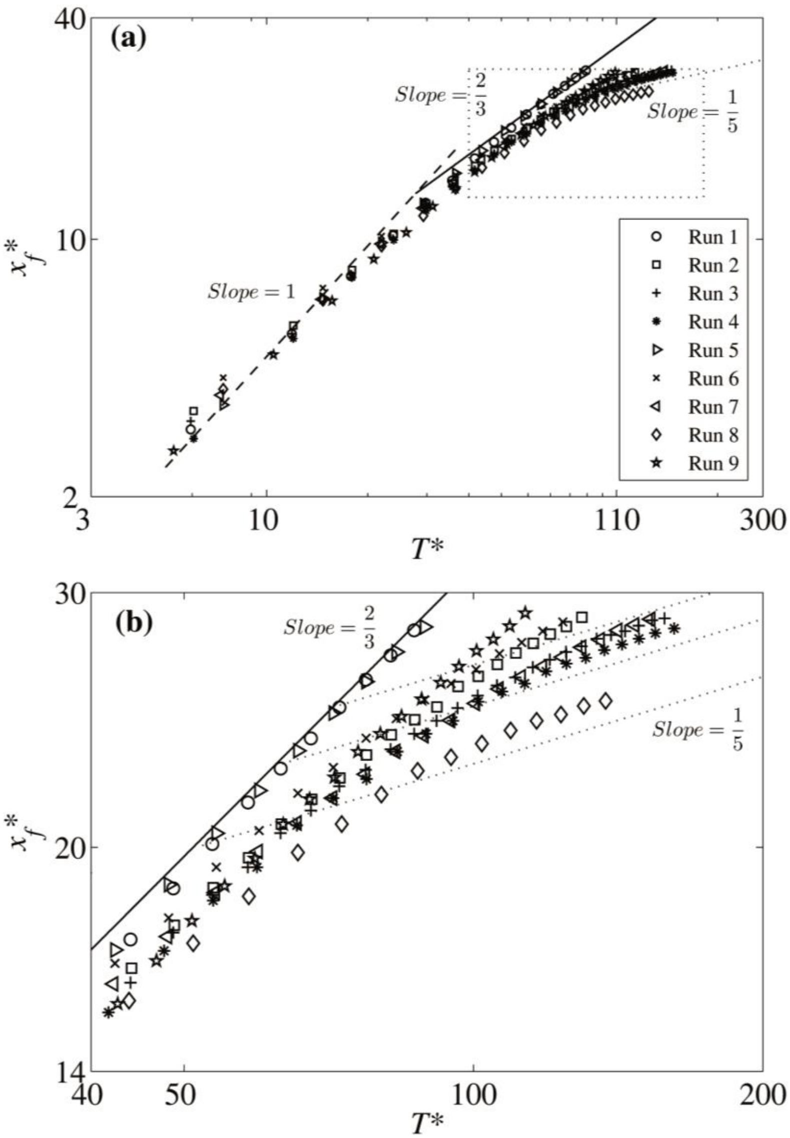

FIG. 6. Dimensionless log-log plot of the experimental front position versus time for all the runs for the whole duration of the experiments (a) and for the temporal interval delimited by the dashed rectangle (b). Dashed line, solid line and dotted line are the theoretical curves for the slumping, self-similar and viscous phase, respectively.

IV. MATHEMATICAL MODEL

Starting from the model of Ref. 5, an improved two-layer, one-dimensional, shallow-water model was developed and benchmarked against new experiments simulating gravity currents moving up a slope. As in Ref. 5, the present model takes into account the entrainment between the two layers and the free surface is modelled as a moving impermeable boundary.

In Figure 7 a sketch of the frame of reference used in the mathematical model is shown. The one-dimensional heavier current of height $h_1(x, t)$ and density ρ_1 flows with velocity V_1 below the lighter layer of height $h_2(x, t)$, density ρ_2, velocity V_2 and bounded at the top by a free surface. θ is the angle formed between the bed of the tank and the horizontal. For the mathematical model, negative values of θ are referred to up sloping angles.

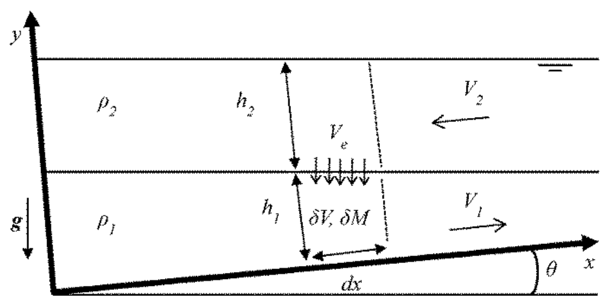

FIG. 7. Frame of reference used in the mathematical model.

The Ref. 5 model is based on the following hypothesis: the density of the ambient fluid ρ_2 is considered to be constant; the density of the dense fluid ρ_1 depends on time, but not on space. In this case at each time step density gradients inside the body of the gravity current are not allowed. The system of the governing equations of the present model is obtained on the basis of Ref. 5 model, by removing the hypothesis of fluid homogeneity and considering ρ_1 as a function of both time and space. Therefore in addition to the equation of mass conservation and the momentum equations projected on the x-axis for both ambient and dense fluid, in the governing equations of the present model a fifth equation appears in order to model the space-time evolution of ρ_1:

$$\begin{cases} \dfrac{\partial(\rho_1 h_1)}{\partial t} + \dfrac{\partial(\rho_1 h_1 V_1)}{\partial x} = \rho_2 V_e \\ \dfrac{\partial(\rho_2 h_2)}{\partial t} + \dfrac{\partial(\rho_2 h_2 V_2)}{\partial x} = -\rho_2 V_e \\ \dfrac{\partial V_1}{\partial t} + \dfrac{\partial}{\partial x}\left[\dfrac{V_1^2}{2} + \left(\dfrac{\rho_2 h_2 + \rho_1 h_1}{\rho_1}\right) g\cos\theta\right] = g\sin\theta - \dfrac{\tau_{1b} + \tau_{21}}{\rho_1 h_1} \\ \dfrac{\partial V_2}{\partial t} + \dfrac{\partial}{\partial x}\left[\dfrac{V_2^2}{2} + \left(\dfrac{\rho_1 h_1}{\rho_1} + \dfrac{\rho_2 h_2}{\rho_2}\right) g\cos\theta\right] = g\sin\theta + \dfrac{\tau_{2b} + \tau_{12}}{\rho_2 h_2} \\ \dfrac{\partial \rho_1}{\partial t} + V_1 \dfrac{\partial \rho_1}{\partial x} = -(\rho_1 - \rho_2)\dfrac{V_e}{h_1} + C_d \dfrac{\partial^2 \rho_1}{\partial x^2} \end{cases} \tag{6}$$

where the unknown quantities are h_1, h_2, V_1, V_2, and ρ_1. The entrainment between the two layers produces a mass flow from the lighter fluid (i.e. the ambient fluid) to the heavier one (i.e. the gravity current). ρ_2 is considered constant, while ρ_1 has to be modelled in order to account for the dilution of the dense fluid, due to the entrained fresh water. Further details about the modelling of $\rho_1 = \rho_1(x, t)$ will be provided hereinafter in this section.

Regarding the stress terms, τ_{1b} and τ_{2b} are the shear stresses due to the rigid boundaries for the dense and the ambient fluid, respectively. These terms include the shear stress due to the bottom and the sidewalls for the lower layer and only the shear stress due to the sidewalls for the upper layer. $\tau_{12} = \tau_{21}$ stands for the shear stress at the interface between the two fluids.

Both τ_{1b} and τ_{2b} are modelled as in Ref. 8:

$$\begin{aligned} \tau_{1b} &= \lambda_1 \rho_1 \frac{V_1|V_1|}{8}\frac{(2h_1 + b)}{b} \\ \tau_{2b} &= -\lambda_2 \rho_2 \frac{V_2|V_2|}{8}\frac{(2h_2)}{b} \end{aligned} \tag{7}$$

where λ_1 and λ_2 are the friction factors for the lower and the upper layer respectively and b is the width of the tank. The definition of λ_i for the i_{th} layer is given, as in Ref. 8, by:

$$\lambda_i = \lambda_{i\infty}\left(1+\frac{8h_i}{\mathrm{Re_i}\varepsilon}\right) \tag{8}$$

where $\lambda_{i\infty}$, $\mathrm{Re_i}$ and ε/h_i are the friction factors for turbulent rough flows, the local Reynolds number and the relative roughness of the i_{th} layer, respectively. The roughness value $\varepsilon = 2 \cdot 10^{-5}$ m for the bottom and the sidewalls was used. $\lambda_{i\infty}$ and $\mathrm{R_i}$ are defined as:

$$\lambda_{i\infty} = \frac{1}{4}\left[\log\left(\frac{3.71h_i}{\varepsilon}\right)\right]^{-2} \tag{9}$$

$$\mathrm{Re_i} = \frac{V_i h_i}{\nu_i} \tag{10}$$

The shear stress at the interface τ_{12} is defined following the relation of Ref. 42 as in Ref. 5:

$$\tau_{12} = \tau_{21} = \lambda_{int}\,\frac{\rho_1+\rho_2}{2}\,\frac{(V_1-V_2)|V_2-V_1|}{8} \tag{11}$$

where the friction factor at the interface λ_{int} is defined as a function of the Reynolds number of the dense fluid $\mathrm{Re_1}$ and it is given by:

$$\lambda_{int} = \frac{0.316}{\mathrm{Re}_1^{0.25}} \tag{12}$$

Concerning the modelling of the entrainment, an improved entrainment coefficient $E=V_e/|V_1-V_2|$, obtained by a modified Ref. 9 formula, is used in the present model and is given by:

$$\frac{V_e}{|V_1-V_2|} = \frac{k\cdot \mathrm{Fr}^2}{\mathrm{Fr}^2+5} \tag{13}$$

The structure of (13) is the same used in Ref. 5, but in this work an improved velocity scale, $|V_1-V_2|$, is used. As discussed in Ref. 5, the entrainment relation of Ref. 9 is not appropriate to predict the entrainment due to a gravity current produced by a lock-release, in which squared densimetric Froude numbers rarely reach values higher than 1.25. In addition, mixing in a density current occurs even at subcritical Froude numbers, as shown in the laboratory experiments of Ref. 43, Ref. 11, Ref. 44 and Ref. 7 and in the numerical experiments of Ref. 38. Consequently, Ref. 9 formula was modified. Details regarding the changes in Ref. 9 relation can be found in Ref. 5. In (13) k is a dimensionless coefficient to be calibrated. The higher is k, the higher is the entrainment velocity. The calibration value of k has to balance both the correct evaluation of the gravity current depth and the good simulation of the front speed of the gravity current. The same calibration value k=0.48 obtained by Ref. 5 was used for all the simulations in this work. The value of the entrainment coefficient, obtained using k=0.48, is in agreement with the entrainment evaluation of Ref. 38, obtained by a Large Eddy Simulation in the same experimental conditions.

Fr is the local densimetric Froude number of the dense fluid and is given by:

$$\mathrm{Fr} = \frac{V_1}{\left(h_1 \frac{\rho_1 - \rho_2}{\rho_1} g \cos\theta \right)^{1/2}} \tag{14}$$

The modelling of both temporal and spatial variation of ρ_1 is provided in the present model by the fifth equation in system (6). The two terms on the left hand side of the last equation are the local variation and the convective transport of ρ_1, respectively. The first and the second term on the right hand side of the last equation of system (6) stand for a sink term and a diffusive term, in which C_d is the diffusive coefficient. In this work the calibration value C_d =0.02 m^2/s was used for all the simulations. Such a value is consistent with the expected order of magnitude of C_d given by:

$$C_d \sim H \cdot V \sim 0.1\,m \cdot 0.1\,m/s \sim 10^{-2}\ m^2/s \tag{15}$$

where H and V are the vertical length scale and the velocity scale of the dense fluid.

The sink term $(\rho_2 - \rho_1)V_e / h_1$ is obtained considering the volume per unit width $\delta V = h_1 \mathrm{d}x$, of mass $\delta M = \rho_1 \delta V$, shown in Figure 7.

Ref. 5 performed the explicit calculation of $\rho_1(t)$ by:

$$\rho_1(t) = \frac{M_1 + \int_0^t dt \int_0^{x_f(t)} \rho_2 V_e dx}{V_1 + \int_0^t dt \int_0^{x_f(t)} V_e dx} \tag{16}$$

where $x_f(t)$ is the instantaneous position of the dense current front, M_1 and V_1 are the mass and volume per unit width, at t=0 of the lower layer and the two integrals are the unit mass and unit volume entering into the lower layer through the interface in the time interval (0,t).

Writing (16) in differential and local form by removing the integral, the local values of density of such a volume at times t and $t + \Delta t$, with Δt suitably small, are given by:

$$\rho_1(x,t) = \frac{\delta M}{\delta V} \tag{17}$$

$$\rho_1(x, t+\Delta t) \cong \frac{\delta M + \rho_2 V_e dx \Delta t}{\delta V + V_e dx \Delta t} \tag{18}$$

The time derivative of ρ_1 is calculated as the limit value of the difference between (18) and (17), divided by Δt, for Δt approaching to zero:

$$\frac{\partial \rho_1}{\partial t} = \lim_{\Delta t \to 0} \left[\frac{\rho_1(x, t+\Delta t) - \rho_1(x,t)}{\Delta t} \right] = (\rho_2 - \rho_1) \frac{V_e}{h_1} \tag{19}$$

The mathematical model was numerically solved by an explicit MacCormack-like finite difference method, with a predictor-corrector scheme, whose details can be found in Ref. 5.

At t=0 the following initial conditions were adopted ($\theta < 0$ for an upslope):

$$h_1(x,0) = \begin{cases} h_0 + x \tan\theta & 0 \le x \le x_0 \\ 0 & x_0 < x \le L \end{cases} \tag{20}$$

$$h_2(x,0) = \begin{cases} 0 & 0 \le x \le x_0 \\ h_0 + x \tan\theta & x_0 < x \le L \end{cases} \tag{21}$$

$$V_1(x,0) = V_2(x,0) = 0 \quad 0 \le x \le L \tag{22}$$

Regarding the boundary conditions, $V_1(0,t)=V_2(0,t)=V_2(L,t)=0$ was imposed, and for the heavier fluid Neumann conditions were applied: the derivative of the density on the x-direction was set equal to zero at x=0 and at the current's front position.

V. COMPARISON BETWEEN LABORATORY EXPERIMENTS AND NUMERICAL SIMULATIONS

A. Time evolution of the gravity current's interface

In order to assess the ability of the proposed model in simulating gravity current dynamics, numerical results, obtained accounting for both temporal and spatial variation of the current density ρ_1, are compared with laboratory measurements and numerical simulations performed by Ref. 5 model, which takes into account the temporal variation of ρ_1 only.

Figures 8 and 9 show the interface between the dense and the ambient fluid predicted by the numerical models overlapped to the images acquired by the camera for Run 1 (i.e. flat bed) and Run 4 (θ=1.52°) at four different instants after the gate removal. For the initial times, a good agreement between experiments and numerical simulations obtained with both the present (solid line) and the Ref. 5 model (dashed-dotted line) can be observed. In particular, during the first stage of development of the gravity current, numerical results agree both in simulating the current's head position, and in reproducing the current's head shape. For the later times shown in Figures 8c-d and Figures 9c-d a better agreement with the laboratory current shape is obtained using the present model. The shape of the current head simulated by the present model is less sharp and more similar to the experimental shape than the one obtained by the Ref. 5 model for the considered instants. This difference in reproducing the current shape can be due to the ability of the present model in simulating the density diffusion process.

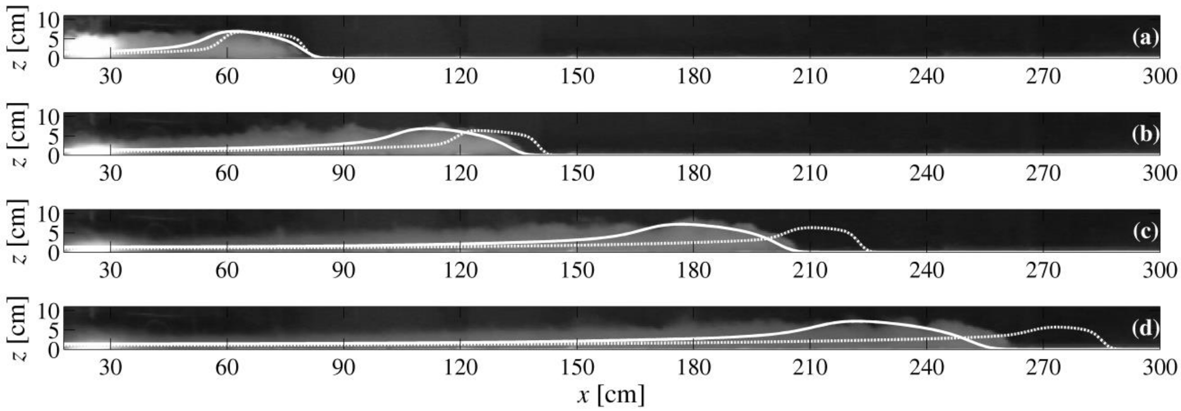

FIG. 8. Comparison of numerical gravity current interface for Run 1 (flat bed) and the images acquired by the camera at four different times: 5.0 s (a), 10.0 s (b), 17.5 s (c), 24.5 s (d); Ref. 5 model (dotted line) and present model (solid line).

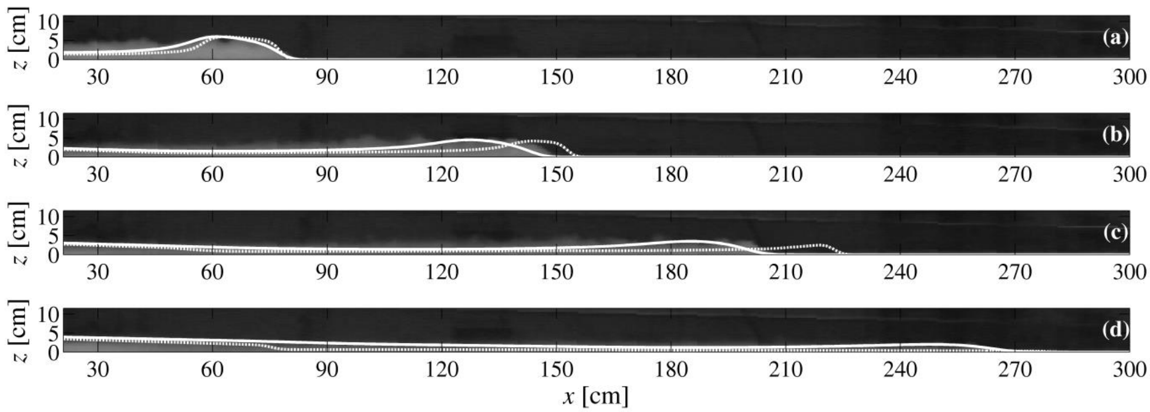

FIG. 9. Comparison of numerical gravity current interface for Run 4 (θ=1.52°) and the images acquired by the camera at four different times: 5.0 s (a), 11.5 s (b), 19.5 s (c), 33.0 s (d); Ref. 5 model (dotted line) and present model (solid line).

In order to quantify the capability of both the present and the Ref. 5 model in reproducing the current shape, a percentage error E_p, based on the difference between the area under the interpolated numerical profile and the area under the interpolated experimental profile, is computed for each time in the following way:

$$E_p = \frac{100}{h_0 L}\int_0^L \left|h_n - h_e\right| dx \tag{23}$$

in which h_n and h_e stand for the interface between the dense layer and the ambient fluid predicted by the numerical simulation and measured by the threshold method, respectively.

In Table III and Table IV computed values of E_p for four different times are shown for Run 1 (i.e. flat bed) and Run 4 (θ=1.52°), respectively. The error E_p for the simulation obtained with the present model is lower than the error computed for the simulation performed by Ref. 5 model for all the considered instants. Therefore the present model is able to reproduce the current shape better than the previous one for both the runs with flat and up sloping beds.

TABLE III. Percentage error E_p. computed for Run 1 (flat bed) on the basis of (23), for the simulations obtained with both the present model and the Ref. 5 model, at four different times.

t (s)	Present model	Ref. 5 model
5.0	4.0	5.4
10.0	6.7	10.1
17.5	10.2	16.9
24.5	11.8	18.8

TABLE IV. Percentage error E_p. computed for Run 4 (θ=1.52°) on the basis of (23), for the simulations obtained with both the present model and the Ref. 5 model, at four different times.

t (s)	Present model	Ref. 5 model
5.0	2.7	3.7
11.5	5.4	7.3
19.5	5.6	10.0
33.0	3.6	8.6

B. Time histories of the front position

In Figure 10 and Figure 11 the dimensionless time histories of experimental front positions are compared to the numerical ones for the runs conducted with ρ_{01}=1060 Kg/m^3 and 1090 Kg/m^3, respectively. The plots show the results obtained by the present model (black lines) and the Ref. 5 model (grey lines). While during the first stage of development of the gravity currents both models agree well with the laboratory data, in the later part of the current evolution a better agreement is observed when the present model is used. The improved ability of the present model in reproducing the gravity currents dynamics is ascribed to the realistic effects produced by the instantaneous spatial density distribution, obtained by solving the fifth equation of system (6).

In order to define the ability of the model in predicting the temporal evolution of the front position, a mean percentage error E_{xf} was computed in the following way:

$$E_{xf} = \frac{100}{N}\sum_{j=1}^{N}\left(\frac{\left|x_{nf,j} - x_{ef,j}\right|}{x_{ef,j}}\right) \qquad (24)$$

in which N is the total number of experimental data and $x_{nf,j}$ and $x_{ef,j}$ are the numerical and experimental j^{th} front position, respectively.

Table V shows E_{xf} for the simulations obtained by the present and the Ref. 5 model for all the runs. For the present model E_{xf} reaches the maximum value of 5.0% in Run 6 and the minimum value of 2.0% in Run 2. Although E_{xf} is of the same order of magnitude in all the simulations, the values are lower in the present model runs than in those obtained with Ref. 5 model for all the runs except for Run 5, which was performed on a flat bed. Therefore the agreement between the numerical results obtained with the proposed model and the measured front position is good, being the error reasonable for all the investigated experimental conditions. In particular, the present model is able to predict the time history of the front position better than Ref. 5 model, especially for gravity currents propagating up a slope.

TABLE V. Mean percentage error E_{xf}. computed for each run on the basis of (24), for the simulations obtained with both the present model and the Ref. 5 model.

Run	Present model	Ref. 5 model
1[a]	2.9	5.0
2	2.0	9.2
3	2.2	6.3
4	3.1	7.8
5[a]	4.8	3.9
6	5.0	6.8
7	3.5	7.1
8	2.6	6.8

[a]Runs performed on flat bed.

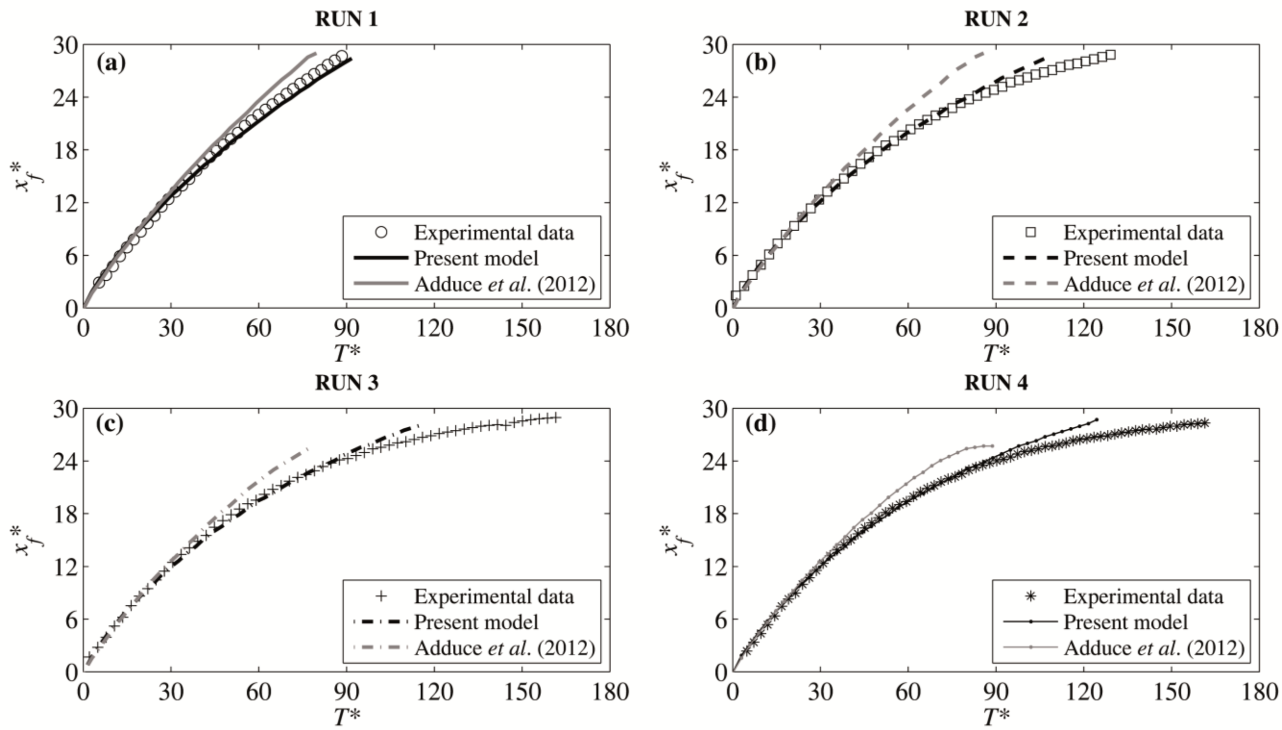

FIG. 10. Comparison of experimental and numerical front position versus time in dimensionless form for Runs 1-4, performed with ρ_{01}=1060 Kg/m^3 and different values of θ: 0.0° (a), 1.14° (b), 1.39° (c) and 1.52° (d), respectively; Ref. 5 model (grey lines), present model (black lines).

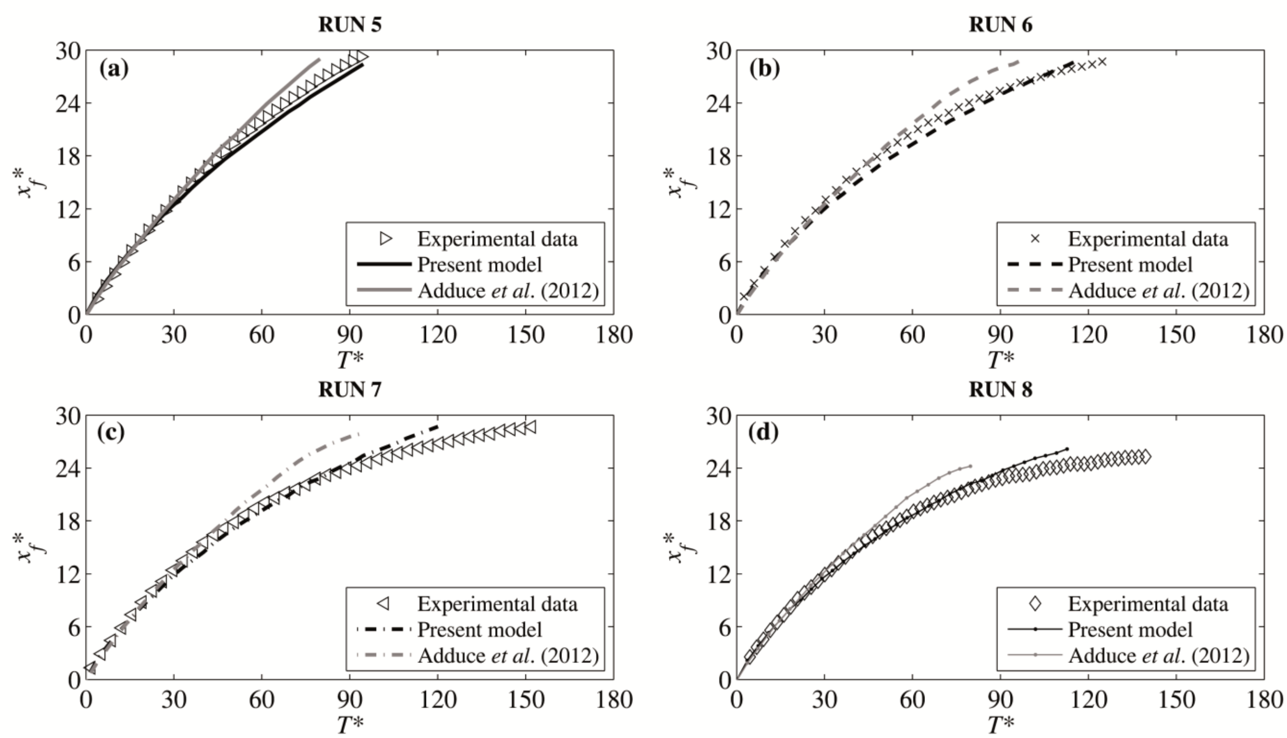

FIG. 11. Comparison of experimental and numerical front position versus time in dimensionless form for Runs 5-8, performed with ρ_{01}=1090 Kg/m^3 and different values of θ: 0.0° (a), 1.39° (b), 1.45° (c) and 1.80° (d), respectively; Ref. 5 model (grey lines), present model (black lines).

C. Streamwise velocity

Figure 12 and Figure 13 show the comparison between the depth averaged streamwise velocity component u measured by PIV and the same velocity component predicted by the present model and the Ref. 5 model at two different times. As the numerical model adopts the shallow-water approximation, in order to compare numerical and experimental results velocity values measured by PIV were depth averaged. Figure 12a and Figure 13a refer to a time at which the current head is within the field of view, while Figure 12b and Figure 13b refer to the time t=34.7 s, during which the tail of the current is visible in both the investigated domains (i.e. Run PIV1 and Run PIV2). Regarding the head of the current, shown in Figure 12a and Figure 13a, a fairly good agreement between the PIV depth averaged measurements and the numerical simulations obtained by both models can be observed. In particular, in the head region (Figure 12a and Figure 13a) while the numerical results obtained by Ref. 5 model provide a steep variation of the depth averaged velocity curve close to the nose of the current, the present model simulation shows a lower slope of the curve at the nose of the current.

In Figure 12b and Figure 13b lower values for both experimental and numerical results of the depth averaged streamwise velocity in the tail region, if compared to the values in the head region (i.e. Figure 12a and Figure 12b) can be observed. Moreover a backflow (i.e. negative values of depth averaged streamwise velocity) occurs in both numerical and measured velocities. Numerical simulations performed by both the present and Ref. 5 model, overestimate the backflow, although such a discrepancy between experimental and numerical results is lower for the simulation obtained by the present model if compared to the results provided by the Ref. 5 model.

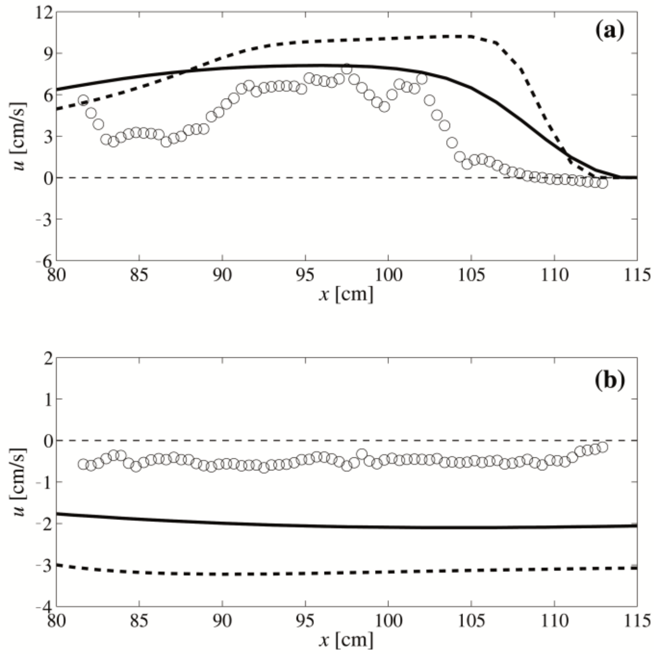

FIG. 12. Depth averaged streamwise velocity of the dense layer versus *x* at *t*=8.4 s (a) and *t*=34.7 s (b): PIV measurements for Run PIV1 (circles), numerical simulations with the present model (solid line) and with Ref. 5 model (dashed line).

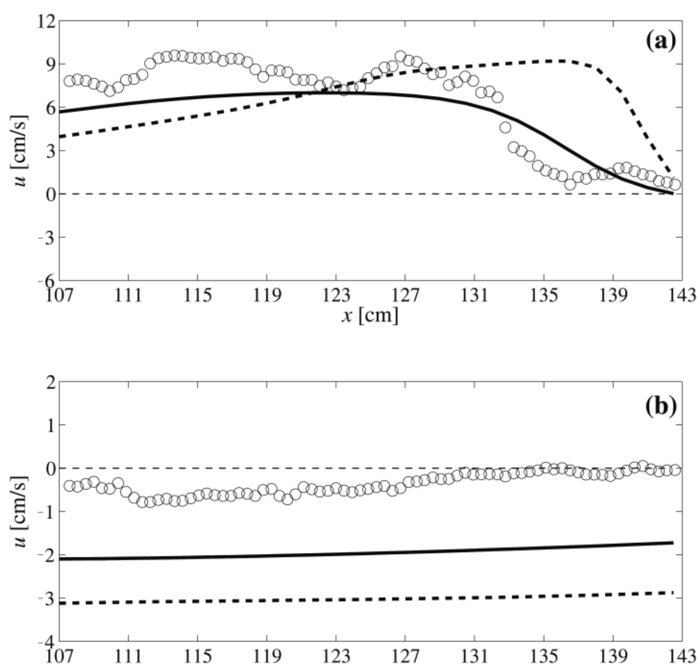

FIG. 13. Depth averaged streamwise velocity of the dense layer versus *x* at *t*=11.8 s (a) and *t*=34.7 s (b): PIV measurements for Run PIV2 (circles), numerical simulations with the present model (solid line) and Ref. 5 model (dashed line).

VI. CONCLUSIONS

The aim of the present work is the study of the dynamics of gravity currents propagating on horizontal and up sloping beds by laboratory experiments and numerical simulations. In particular laboratory experiments are used as a benchmark to validate the shallow-water model presented in this work.

Eight lock-exchange release experiments were carried out keeping constant both the initial volume of the lock fluid and the density of the ambient fluid and testing two different values of the initial density of the heavier fluid and four values of the bed upslope. The movie of each experiment was acquired by a digital camera and a threshold method was applied in order to detect the interface between the gravity current and the ambient fluid. The flow features of a gravity current, i.e. a head and a tail region, are recognized in the laboratory runs performed on flat and up sloping beds, while an accumulation of dense fluid in the lock region of the tank is observed only for the gravity currents flowing up a slope. As expected, a decrease of the current speed is observed as the bed upslope increases.

Experimental results are compared with theoretical laws for front evolution given by previous studies. While the slumping phase and the self-similar phase are observed to occur for gravity currents propagating on both flat and up sloping beds, only the currents flowing up a slope show a viscous phase-like behavior in the last stage of the experiment. In particular, the runs with the highest values of the up sloping angle seem to develop the viscous phase. The slope of the curve of the dimensionless front position versus dimensionless time is in agreement with the theoretical prediction.

Numerical simulations were performed using both the Ref. 5 model and the present shallow-water model. As in Ref. 5, the present model takes into account the free surface and the entrainment between the two fluids. While Ref. 5 model is based on the hypothesis of fluid homogeneity, accounting for the temporal variation of the gravity current density and neglecting its spatial variations, in the present model the space-time evolution of the gravity current density is modelled.

The ability of both the present and the Ref. 5 model in simulating the gravity current shape and the front position versus time was tested. For flat and up sloping beds the present model is able to simulate the gravity current head position and the shape during the whole duration of the experiment, while Ref. 5 model agrees with laboratory measurements only during the first stage of development of the gravity current. In addition, the present model is able to predict the front position better than the Ref. 5 model, especially for gravity currents travelling up a slope. For these gravity currents a backflow region develops close to the lock position, as shown by laboratory experiments and numerical simulations as well. Both models predict the presence of the backflow region but the simulations overestimate negative values of the depth-averaged streamwise velocity.

In conclusion the present model is able to simulate the dynamics of gravity current better than Ref. 5 model. The ability of the present model in both reproducing the gravity current shape and predicting the position of the gravity current nose, mostly appreciable for the experiments performed up a slope, can be ascribed to its capability in simulating density gradients in the streamwise direction.

ACKNOWLEDGMENTS

C.A. acknowledges financial support through the University Roma Tre grant “Gravity currents: laboratory experiments and mathematical modelling”. M.L.R. acknowledges financial support through the research grant PRIN 2010-2011.

REFERENCES

[1]J.E. Simpson, *Gravity currents in the environment and the laboratory* (Cambridge University Press, Cambridge, 1997).

[2]H.E. Huppert, J.E. Simpson, "The slumping of gravity currents" J. Fluid Mech. 99, 785 (1980).

[3]B.M. Marino, L.P. Thomas, P.F. Linden, "The front condition of gravity currents" J. Fluid Mech. 536, 49 (2005).

[4]M. Ungarish, "Axysimmetric gravity currents at high Reynolds number: on the quality of shallow-water modelling of experimental observations" Phys. Fluids 19, 033602 (2007).

[5]C. Adduce, G. Sciortino, S. Proietti, "Gravity currents produced by lock-exchange: experiments and simulations with a two layer shallow-water model with entrainment" J. Hydraulic Eng. 138, 111 (2012).

[6]H.I.S Nogueira, C. Adduce, E. Alves, M.J. Franca "Analysis of lock-exchange gravity currents over smooth and rough beds" J. Hydr. Res. 51, 417 (2013b).

[7]H.I.S Nogueira, C. Adduce, E. Alves, M.J. Franca "Dynamics of the head of gravity currents" Environ. Fluid Mech. 14 (2014a).

[8]M. La Rocca, C. Adduce, G. Sciortino, A. Bateman Pinzon, "Experimental and numerical simulation of three-dimensional gravity currents on smooth and rough bottom" Phys. Fluids 20, 106603 (2008).

[9]T.H. Ellison, J.S. Turner, "Turbulent entrainment in stratified flows" J. Fluid Mech. 6, 423 (1959).

[10]R.E. Britter, J.E. Simpson, "Experiments on the dynamics of a gravity current head" J. Fluid Mech. 89, 223 (1978).

[11]C. Cenedese, C. Adduce, "Mixing in a density driven current flowing down a slope in a rotating fluid" J. Fluid Mech. 604, 369 (2008).

[12]S.K. Ooi, G. Costantinescu, L.J. Weber, "2D large-eddy simulation of lock-exchange gravity current flows at high Grashof numbers" J. Hydraul. Eng. 133, 1037 (2007).

[13]S.K. Ooi, G. Costantinescu, L.J. Weber, "Numerical simulations of lock-exchange compositional gravity current" J. Fluid Mech. 635, 361 (2009).

[14]F.A. Bombardelli, M.I. Cantero, M.H. Garcia, G.C. Buscaglia, "Numerical aspect of the simulation of discontinuous saline underflows: the lock-exchange problem" J. Hydraul. Res. 47, 777 (2009).

[15]C. Härtel, E. Meiburg, F. Necker, "Analysis and direct numerical simulation of the flow at a gravity current head – Part 1: Flow topology and front speed for slip and no-slip boundaries" J. Fluid Mech. 418, 189 (2000a).

[16]C. Härtel, F. Carlsson, N. Thunblom, "Analysis and direct numerical simulation of the flow at a gravity current head – Part 2: The lob-and-cleft instability" J. Fluid Mech. 418, 213 (2000b).

[17]M. Cantero, S. Balachandar, M. García, J. Ferry, "Direct numerical simulations of planar and cylindrical density currents" J. Appl. Mech. 73, 923 (2006).

[18]M. Cantero, J. Lee, S. Balachandar, M. García, "On the front velocity of gravity currents" J. Fluid. Mech. 586, 1 (2007).

[19]G. Gerber, G. Diedericks, G.R. Basson, "Particle image velocimetry measurements and numerical modeling of a saline density current" J. Hydraul. Eng. 137, 333 (2011).

[20]M. La Rocca, C. Adduce, V. Lombardi, G. Sciortino, R. Hinkelmann, "Development of a Lattice Boltzmann Method for two-layered shallow-water flow" Int. J. Numer. Meth. Fluids. 70, 1048 (2012a).

[21]P. Prestininzi, G. Sciortino, M. La Rocca, "On the effect of the intrinsic viscosity in a 2-layer Shallow Water Lattice Boltzmann Model of axisymmetric density currents" J. Hydraul. Res. 51, 668 (2013).

[22]M. La Rocca, P. Prestininzi, C. Adduce, G. Sciortino, R. Hinkelmann, "Lattice Boltzmann simulation of 3D gravity currents around obstacles" Int. J. Offshore Polar. Eng 23, (2013).

[23]T.B. Benjamin, "Gravity currents and related phenomena" J. Fluid. Mech. 31, 209 (1968).

[24]J.W. Rottman, J.E. Simpson "Gravity currents produced by instantaneous release of a heavy fluid in a rectangular channel" J. Fluid. Mech. 135, 95 (1983).

[25]J.O. Shin, S.B. Dalziel, P.F. Linden, "Gravity currents produced by lock exchange" J. Fluid. Mech. 521, 1 (2004).

[26]M. La Rocca, C. Adduce, G. Sciortino, A. Bateman Pinzon, M.A. Boniforti, "A two-layer, shallow water model for 3D gravity currents" J. Hydraul. Res. 50, 208 (2012b).

[27]R.E. Britter, P.F. Linden, "The motion of the front of a gravity current travelling down an incline" J. Fluid. Mech. 99, 531 (1980).

[28]T. Maxworthy, R.I. Nokes, "Experiments on gravity currents propagating down slopes. Part 1. The release of a fixed volume of heavy fluid from an enclosed lock into an open channel" J. Fluid. Mech. 584, 433 (2007).

[29]C. Cenedese, C. Adduce, "A new entrainment parameterization for mixing in overflows" J. Phys. Oceanogr. 40, 1835 (2010).

[30]P.G. Baines, "Mixing in downslope flows in the ocean – plumes versus gravity currents" Atmos Ocean. 46, 405 (2008).

[31]A. Dai, "Modified thermal theory for gravity currents on sloping boundaries" J. Hydraulic Eng. 136, 826 (2010).

[32]A. Dai, "Gravity currents from instantaneous sources down a slope" J. Hydraulic Eng. 138, 237 (2012).

[33]A. Dai, "Experiments on gravity currents propagating on different bottom slopes" J. Hydraulic Eng. 731, 117 (2013).

[34]T. Maxworthy, "Experiments on gravity currents propagating down slopes. Part 2. The evolution of fluid released from closed locks into a long, open channel" J. Fluid. Mech. 647, 27 (2010).

[35]A.S. Safray, I.V. Tkachenko, "Numerical modeling of gravity currents in inclined channels" Fluid. Dyn. 44, 22 (2009).

[36]B.R. Sutherland, D. Polet, M. Campbell, "Gravity currents shoaling on a slope" Phys. Fluids 25, 086604 (2013).

[37]L.J. Marleau, M.R. Flynn, B.R. Sutherland, "Gravity Currents Propagating Up a Slope" Phys. Fluids 26, 046605 (2014).

[38]L. Ottolenghi, C. Adduce, R. Inghilesi, F. Roman, V. Armenio, in *Proceedings of the International Conference on Fluvial Hydraulics (River Flow 2014)*, Lausanne, Switzerland, 3-5 September 2014, edited by A.J. Schleiss, G. De Cesare, M.J. Franca, M. Pfister (Taylor & Francis Group, London, 2014), p. 36.

[39]H.I.S Nogueira, C. Adduce, E. Alves, M.J. Franca, "Image analysis technique applied to lock-exchange gravity currents" Meas. Sci. Technol 24, 047001 (2013a).

[40]A. Alahyari, E.K. Longmire, "Particle image velocimetry in a variable density flow: application to a dynamically evolving microburst" Exp. Fluids. 17, 434 (1994).

[41]H.E. Huppert, "The propagation of two-dimensional and axisymmetric viscous gravity currents over a rigid horizontal surface" J. Fluid. Mech. 121, 43 (1982).

[42]G. Supino, *Manuale dell'Ingegneria Civile* (Edizioni Scientifiche A. Cremonese, Rome, 1981).

[43]C. Cenedese, J.A. Whitehead, T.A. Ascarelli, M. Ohiwa, "A dense current flowing down a sloping bottom in a rotating fluid" J. Phys. Oceanogr. 34, 188 (2004).

[44]A.T. Fragoso, M.D. Patterson, J.S. Wettlaufer, "Mixing in gravity currents" J. Fluid. Mech. 734, R2 (2013).